International Journal of Mining Science and Technology 35 (2025) 1663–1676

Contents lists available at ScienceDirect

International Journal of Mining Science and Technology

journal homepage: www.elsevier.com/locate/ijmst

Anisotropy of laser-induced electro-response in shale: Modelling and experimental validation

Xuecong Liu, Zhengchun Hong, Yuqi Jiao, Kun Zhao *, Xinyang Miao

Key Laboratory of Oil and Gas Terahertz Spectroscopy and Photoelectric Detection, Petroleum and Chemical Industry Federation, China University of Petroleum-Beijing, Beijing 102249, China

ARTICLE INFO

Article history:
Received 13 May 2025
Received in revised form 16 August 2025
Accepted 24 August 2025
Available online 30 October 2025

Keywords:
Laser-induced electro-response
Shale
Anisotropy
Laser-thermal effect
Polarization electric field
Laser-induced plasma

ABSTRACT

Laser-induced electro-response (LIER), as a new method that complements conventional rock physics testing techniques, is expected to address issues such as of unclear mechanisms, model deficiency, inconsistent evaluation parameters, and difficulty in separating multiple coupling factors in shale anisotropy evaluation, and establish a more complete and reliable shale physical property evaluation system. A testing strategy for out of plane anisotropy (OPA) was proposed for characterising anisotropy by LIER, where the near infrared (NIR) continuous laser (CL) and nanosecond pulsed laser (PL) were used to irradiate the surface of oblique cut shale, and the transverse LIER of the surface was measured. A LIER detection model is constructed from the laser-thermal effect, residual transverse polarization electric field and thermionic emission transport mechanism, which is strongly relying on laser power, bias voltage, and inclination angle of the measurement direction relative to the bedding plane of shale. For OPA test on the slice of oblique cut shale under CL irradiation, the relationship between the product of LIER simulation parameters and the tilting angle can be described by a cubic function and an impulse function with a maximum value at the threshold angle. In addition, the thermal accumulation and transient thermal effects are induced in the shale under a high-energy short laser pulse irradiation, and the simulation results indicate that there is an exponential relationship between the product of parameters in the LIER model and the tilt angle. Thus, for OPA test under CL and PL irradiations, it is recommended to use the product of parameters as an evaluation index for shale anisotropy. Furthermore, to solve the problem of multiple influencing factors entangled in the exponential term of the LIER model, the tangential LIER measurement was performed on the side of cylindrical shale core, where the provided LIER model effectively presented the anisotropy of tight shale plug, especially the effects of bias voltage and laser power on LIER were relatively separated as independent variables. Finally, the LIER at the end of laser drilling is presented well using the optimized model under a focused ns NIR PL irradiation, indicating that LIER is expected to be a real-time means for characterizing shale anisotropy during laser drilling processes. These results show that the present work is fundamental for the precise evaluation and effective development of anisotropic shale reservoirs, and will drive the advances of LIER in the exploration for shale oil and gas.

© 2025 China University of Mining & Technology. Publishing services by Elsevier B.V. This is an open access article under the CC BY-NC-ND license (http://creativecommons.org/licenses/by-nc-nd/4.0/).

1. Introduction

Shale oil and gas is a resource-rich clean energy and mainly located in sedimentary and metamorphic rock formations. Shales are not only a reservoir rocks with the ability to seal carbon dioxide, methane, etc., but also a source rocks [1]. Unlike conventional sandstone reservoirs, shales exhibit distinct bedding planes which are caused by preferentially orientated of clay minerals and organic matter [2]. Lamination is the most frequently cited influencing factor for shale anisotropy, which leads to different electrical, mechanical, thermal, seismic, and magnetic properties at directions parallel and perpendicular to their bedding planes, and has significant impact on energy industry and the research of geophysical properties in the Earth. Traditional techniques such as magnetic susceptibility, seismic, mechanical, and geo-electrical response detections can reveal post-depositional anisotropic characteristics of shales with invisible bedding. The seismic anisotropy parameters can describe uniform rock properties along the layering and a bed-by-bed variation of rock properties [3,4]. The anisotropy of magnetic susceptibility can reveal the orientation

---

* Corresponding author.
E-mail address: zhk@cup.edu.cn (K. Zhao).

https://doi.org/10.1016/j.ijmst.2025.08.015
2095-2686/© 2025 China University of Mining & Technology. Publishing services by Elsevier B.V.
This is an open access article under the CC BY-NC-ND license (http://creativecommons.org/licenses/by-nc-nd/4.0/).

structure and sedimentary characteristics of rocks [5]. The colinear electrode arrays, electrical image logging, and many electrical detection techniques focus on the qualitative identification of shale laminae [6]. Based on hydraulic fracturing and drilling engineering requirements, mechanical characteristic parameters are typically used to characterize the strength characteristics of shale anisotropy [7,8]. At the macro scale, these detection technologies each have their own characteristics and application advantages. In addition, the shale anisotropy in microscale was probed by small-angle neutron scattering [9], 3D X-ray computed tomography [10], and peak force-tunneling atomic force microscopy [11].

Due to the multiple influences of geological conditions and types, the quantitative evaluation and generation mechanism of shale anisotropy is complex, and a single research method is insufficient to establish a more complete and reliable rock physical property evaluation system [12]. Furthermore, shale's inherent structural instability and complex physicochemical properties present significant challenges for obtaining complete cores and acquiring reliable well logs in horizontal wellbore sections [13,14]. Therefore, it is necessary to develop new evaluation and detection frameworks by integrating multiple research methods to handle complex samples, which can greatly eliminate the influence of uncertain factors in the interpretation and evaluation process. With the advancement of nonlinear optics, laser-based detection has become a transformative alternative through direct photon-matter interaction [15], which was applied in various aspects of exploration, production, and refining processes of oil and gas industry. For example, due to the high resistance properties of shale, it is difficult to directly measure the electrical anisotropy of shale with conventional DC power supply. However, laser irradiation can reduce the resistivity of high resistance shale by four orders of magnitude and provides additional information on the nature of shales [16]. Moreover, high-power continuous wavelength laser and high-energy pulsed lasers were also used for breaking and drilling rocks in oil and gas exploration to improve drilling efficiency and reduce costs [17,18].

When a laser beam irradiates the surface of high-resistance rock mineral, various physical phenomena occur, including reflection, absorption, energy conversion, heating, melting and gasification, damage and destruction, mechanical effect, plasma, etc. If an electric field inside the material or an external electric field is applied, an induced current or voltage can be detected in the external circuit. Therefore, we combined optical stimulation with real-time electrical signal acquisition to develop laser-induced electro-response (LIER) technique, such as a laser-induced current (LIC) or laser-induced voltage (LIV), and establish a multi-physical field coupling characterization framework for shale by introducing optical characteristics [19]. Previous research has shown that the inflection point of LIV corresponds to the bedding position of shale [20]. In the absence of an external electric field, the LIV of tight shale exhibits a trigonometric relationship with bedding angle [21]. It is the bedding structure of shale to result in significantly higher amplitudes of LIV along the bedding direction than perpendicular to it [22]. When an external bias is applied, the LIV on the side of the insulating shale columnar core is minimized at the center between the electrodes [23]. In addition, when high-energy laser irradiates on the shale, plasma is generated on the shale surface, and the LIV is 180° symmetric and elliptical in polar coordinates, with the long and short axes parallel and perpendicular to the bedding direction, indicating the anisotropic characteristics of shale [24].

As discussed earlier, LIER, as an emerging anisotropic detection method, introduces optical characteristics as a new dimension parameter for evaluating shale anisotropy and has the characteristics of no chemical treatment, simplicity, fast real-time, and low cost, which is also expected to be a new selection to characterize the laser drilling process and reservoir in real time. However, due to the complex interaction between laser and shale, LIER is still in its infancy and faces some challenges in evaluating shale anisotropy, such as a lack of detection models, inconsistent evaluation parameters, and difficulty in effectively separating multiple coupling factors. In this article, to address the above problems, we proposed an out of plane anisotropy (OPA) strategy, where anisotropy is characterized by measuring LIER on the surface of oblique cut shale. The corresponding LIER theory was constructed to enhance the LIER technology system, based on the laser-thermal effect, residual transverse polarization electric field and thermionic emission transport mechanism. The given LIER detection model characterized the OPA of oblique shale slices under near-infrared (NIR) continuous laser (CL) and pulsed laser (PL) irradiation. In addition, the LIER model was optimized to evaluate the anisotropy of cylindrical tight shale cores and the anisotropy of shale during laser drilling.

2. Materials and method

2.1. Sample preparation

The prepared shale samples, namely kerogen-rich, were taken from the outcrop of the Huadian formation in Songliao Basin. The shale is composed of clay, quartz, pyrite feldspar and calcite. X-ray fluorescence (XRF) test revealed that the major elements of the shale sample are Si (23.4%), Ca (11.1%), Fe (7.81%), Al (7.29%), Mg (1.44%), K (1.24%) and S (1.21%). These samples are grayish-brown with a smooth surface without fracture. The experiment focuses on shale with a layered structures as the research object. Scanning electron microscopy (SEM) images show that the shale sample have a typical parallel bedding plane, organic matter exhibits elongation parallel with bedding planes direction, and clay minerals, consisting of feldspar, mica, pyrite, etc., distribute as folded layers (Fig. 1a).

Smaller cubes (10 mm × 7.5 mm × 5 mm) with different bedding angles (θ) were trimmed from the large sample block for subsequent testing and characterization. As shown in Fig. 1b, shale samples are cut at θ=0°, 15°, 30°, 45°, 60°, 75° and 90° with an angular error of less than 2°. The bedding planes are dipping at an angle θ, which denotes the angle between the bedding direction (l) on the front side of the sample and the horizontal direction (//), and the t-direction is inclined with respect to the surface normal (n) by θ. In order to ensure the accuracy of the experimental results, three samples of the same size were cut at each angle. Next, the sample end faces are ground parallel by grinder, ensuring compliance with the preparation standards recommended by subsequent silver electrodes. Two colloidal silver electrodes with 2 mm × 7.5 mm size and a spacing of ~6 mm, are applied to inject bias and prob electrical signal.

2.2. Laser induced electro-response testing

The LIER test system (Fig. 1c) combines a laser source, a LIER signal receiving unit, a laser energy or power meter and the infrared (IR) thermographic system. A 50/50 beam splitter (BS) splits the laser beam to form two beams. One beam of laser irradiated on the surface of the shale and the other beam irradiated in the detector for probing the laser energy and power, which is used to monitor laser energy and power change. The LIER signal receive unit contains a specimen stage, Keithley 2400 Source Meter and computer with data collection software. The bias voltage V_b in this testing system is provided by Keithley 2400. The IR thermal camera (UNI-T, Uti260B; Spectral bandwidth: 8–14 μm, Accuracy: ±2 °C,

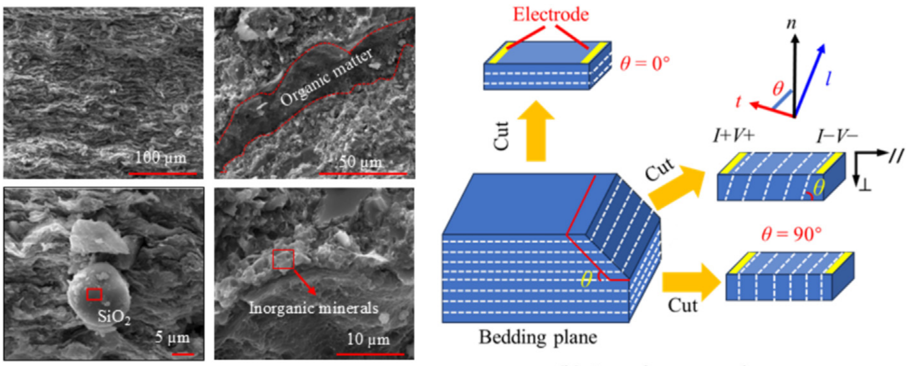

(a) SEM images

(b) Sample preparation

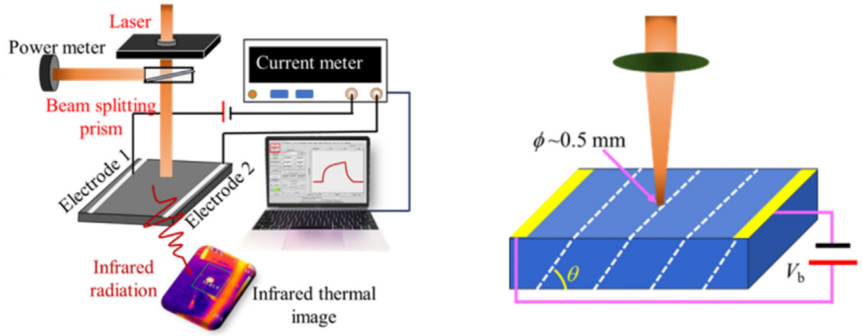

(c) CL and PL irradiation

(d) Laser drilling process

Fig. 1. Sample preparation and LIER testing.

Resolution: 256×192 pixels, Maximum thermal sensitivity: 60 mK) combines temperature image and data by computer software (UTi-Live Screen) to measure temperature changes on the surface of shale. In this work, each sample was tested for three times under identical experimental conditions to ensure result accuracy.

Our previous reports demonstrated that the laser-induced thermal effect played a main role in the LIER signals under NIR laser irradiation [19]. In this work the LIER detection model is specifically designed around and focuses on the laser-induced thermal effect as the primary mechanism. Therefore, NIR lasers, such as 808 and 1064 nm, were selected to ignore the photoelectric effect's contribution [25]. Since laser power (P) significantly influences the LIER response rate and low laser power can cause the testing system unable to detect the LIER signal from the shale, one laser source of 808 nm CL with a spot area of 30π mm^2 was applied to irradiate the shale surface, and the laser power was adjusted from 1.5 to 3.5 W.

The short laser pulses have been extensively investigated to meet the needs of laser drilling research, including millisecond (ms), ns and femtosecond (fs) laser [18]. In the case of fs pulses, thermal diffusion into the surrounding shale bulk material can be neglected, while heating of the surface takes place during the whole pulse duration in the case of ns pulses due to laser-induced thermal effects. Thus, in this work, a Nd:YAG laser (EKSPLA Company) was applied as the PL source, with wavelength (λ) of 1064 nm, pulse duration (τ) of 5 ns, pulse frequency (f) of 10 Hz, pulse energy of 5 mJ, and a laser spot diameter (ϕ) of ~10 mm. As for laser drilling testing, the above short pulse laser with a single-pulse energy of 70 mJ is focused by a lens and the laser spot with a diameter of ~0.5 mm is on the center between the two-parallel-strip electrodes for OPA configuration (Fig. 1d). In fact, the pulse width of ns lasers, from a few ns to tens of ns, has an impact on LIER, and detailed research will be conducted in the future.

3. Principle of LIER detection method

It is approximated that physical parameters such as electrical conductivity σ, thermal conductivity κ, thermal diffusion coefficient D, and absorption A are uniform on the shale laminar surface and vary in the direction perpendicular to that laminar surface. The parameters parallel and perpendicular to the bedding plane are referred to as σ_l, κ_l, D_l, σ_t, κ_t, D_t, respectively. Inset of Fig. 2a shows a schematic diagram of the OPA test, with two strip electrodes parallel to each other. In anisotropic half-space, the electric field distribution between the bar electrodes can be approximated as a parallel electric field, and the parallel surface conductivity σ along the direction of electrodes depends on the direction of the measurement array, which is presented by

$$\sigma = \sigma_t\left(\frac{\sigma_l}{\sigma_t}\cos^2\theta + \sin^2\theta\right) \propto n_\sigma\cos^2\theta + \sin^2\theta \tag{1}$$

where $n_\sigma = \sigma_l/\sigma_t$.

When a laser with a power of P irradiates the surface of a slanted sample with a thickness of d, the sample surface temperature rapidly rises, resulting in a temperature gradient $\nabla_\perp T = \Delta T_p/d$ at the surface and bottom of the sample, $\Delta T_p = T_p - T_0 = \alpha t_p^{1/2} \propto \alpha$, and

$$\alpha = \frac{2PA\sqrt{D_\perp}}{\sqrt{\pi}\,\kappa_\perp} = \frac{2PA}{\sqrt{\pi\rho c_0}\sqrt{\kappa_\perp}} \propto \frac{PA}{\sqrt{\kappa_\perp}} \tag{2}$$

where ρ, c_0, T_0, t_p and T_p are mass density, specific heat, ambient temperature, duration of laser irradiation, surface temperature at the end of laser irradiation, respectively [19]. According to tensor properties, the surface-perpendicular thermal conductivity $\kappa_\perp$ can be presented as

$$\kappa_\perp = \kappa_l\sin^2\theta + \kappa_t\cos^2\theta = \kappa_t\left(\frac{\kappa_l}{\kappa_t}\sin^2\theta + \cos^2\theta\right) \propto n_\kappa\sin^2\theta + \cos^2\theta \tag{3}$$

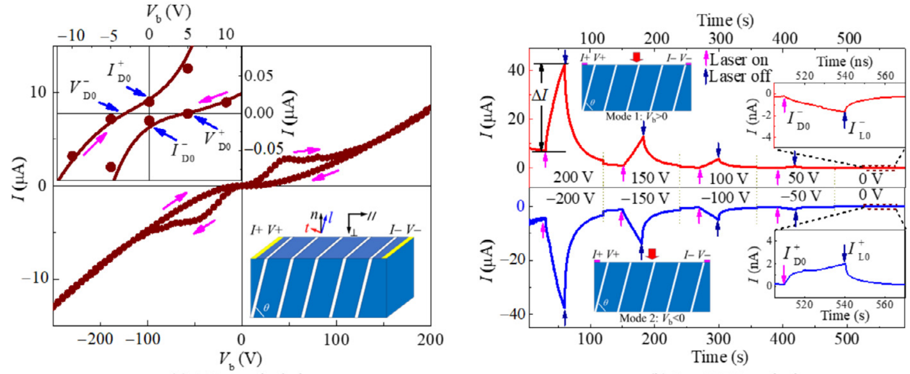

(a) *I-V* curve in dark (b) Two LIER methods

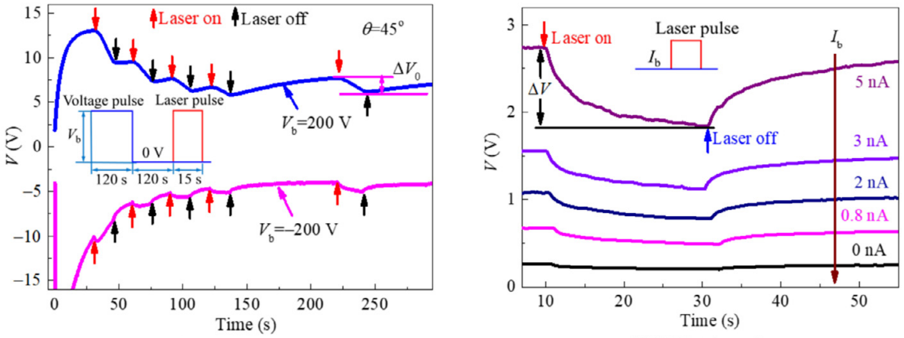

(c) LIER at I_b=0 (d) LIER at lower I_b

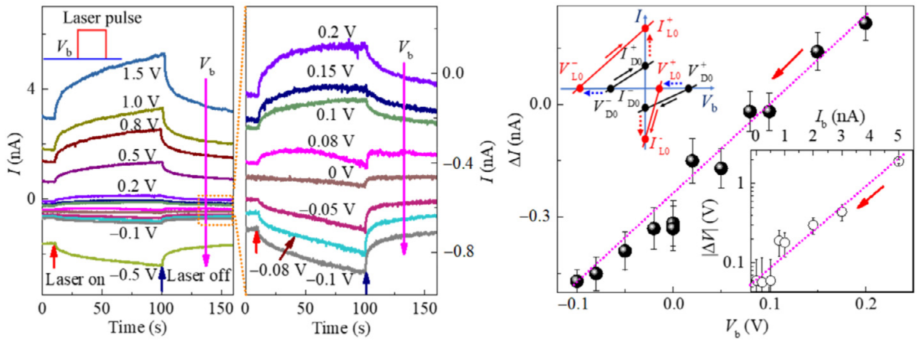

(e) LIER at lower V_b (f) ΔI-V_b and ΔV-I_b

Fig. 2. Typical *I-V* curve and LIER measurements at a tilting angle of θ=45° under the 808 nm laser irradiation with a power of 3.0 W.

where $n_\kappa=\kappa_\parallel/\kappa_\perp$.

Considering the surface of shale as an infinitely thin planar heat source under CL irradiation, the evolution of the surface temperature T and LIC can be represented using the photo-thermal modelling approach as [19]

$$\ln(\mathrm{LIC})=\begin{cases} a_1\ln(\alpha t^{1/2})+b_1 & (0\le t<t_p) \\ a_2\ln\left\{\alpha\left[t^{1/2}-(t-t_p)^{1/2}\right]\right\}+b_2 & (t\ge t_p)\end{cases} \tag{4}$$

Thus, at the end of the laser irradiation time, the change in LIC due to the laser-thermal effect, named as ΔI_H, satisfies the formula as follows:

$$\ln(\Delta I_H)\propto\ln(\Delta T_p)=\ln(T_p-T_0)=\ln(\alpha\sqrt{t_p})\propto\ln\alpha \tag{5}$$

Then, taking anisotropy of conductivity

$$\Delta I_H\propto\frac{\sigma b}{a}\alpha\propto\sigma\alpha\propto\sigma\frac{PA}{\sqrt{\kappa_\perp}} \tag{6}$$

where a is the electrode spacing, and b the current cross-sectional area.

Fig. 2a presented the hysteresis current-voltage (*I-V*) curve of an untilting oil shale (θ=0°) in dark. When the voltage is from +200 to 0 V, the shale is in a high-resistance state (HRS). With the voltage changes from positive to negative, the shale changes from HRS to low-resistance state (LRS), and gradually transforms to HRS after a turning voltage of ~−45 V. When the voltage is scanned from −200 to 0 V, the shale is in HRS again. And then, when the voltage is swept from 0 to +200 V, the shale is first in the LRS, and gradually changes to the HRS to complete a voltage cycle after a transition voltage of ~45 V. It can be seen that the shale switches between LRS and HRS when the voltage polarity is changed with the short-circuit currents (I_{D0}^+ and I_{D0}^-) and open-circuit voltages (V_{D0}^+ and V_{D0}^-) due to residual transverse polarization electric field E_P. The bipolar behavior indicates that the resistance mechanism of shale is an interface type (Supplementary materials) [26].

Fig. 2b displays the LIER measurements of shale at a tilting angle of θ=45° under the 808 nm laser irradiation of a power of 3.0 W, where the bias voltage V_b scans from 200/−200 to 0 V with a spacing 50 V, named as Mode1/Mode 2. The change in LIC at the end of the laser irradiation time, ΔI, monotonically decreased from

36.4 and –37.3 μA at V_b=200 and –200 V, 11.1 and –12.8 μA at V_b=150 and –150 V, 3.6 and –4.5 μA at V_b=100 and –100 V, to 0.7 and –1.1 μA at V_b=50 and –50 V, respectively. It is clear that the short-circuit current was enhanced from I_{D0}^{-} (–0.17 nA) to I_{L0}^{-} (–1.67 nA) for V_b>0 (Mode 1) and I_{D0}^{+} (0.23 nA) to I_{L0}^{+} (2.03 nA) for V_b<0 (Mode 2), respectively, under NIR CL irradiation. In addition, time-dependence of LIER at I_b=0 after 120 s of electric voltage excitation indicates that laser-induced open-circuit voltage ΔV_0 is 1.85 and –1.02 V for V_b=200 and –200 V (Fig. 2c).

Figs. 2d and e display the time-dependence of the measured voltage V and current I under the irradiation of 808 nm-laser with P=3.0 W for θ=45°, at much lower excitation electric currents (I_b ranging from 5 to 0 nA) and voltages (V_b ranging from 1.5 to –0.5 V). The ΔV refers to the change in LIV at the end of the laser irradiation time. Fig. 2f reviews the dependences of ΔI and ΔV on lower V_b and I_b. It is founded that ΔI and ΔV are ~–0.26 nA at V_b=0 and ~–0.065 V at I_b=0, from the fitting curves of ΔI=–0.26 +1.68V_b and ΔV≈–exp(2.73+0.69I_b), respectively. These facts indicates that the residual polarization effect plays a great role in LIER of shale, which was further confirmed by Supplementary materials.

Shale can be abstracted as a multi-layer superposition of parallel dielectric plates. According to classical electromagnetic field theory, the E_P along electrode directions is proportional to $\sin^2\theta$ for a dielectric uniformly distributed between electrodes (Supplementary materials). Due to complex sedimentary and diagenetic processes, shale exhibits a high degree of heterogeneity in terms of composition, pores, fractures, and matrix. These facts result in fluctuations in the angle θ in the relation of $E_P \propto \sin^2\theta$. If the fluctuation in the θ are ignored in this formula, the power of $\sin\theta$ is no longer a definite value of 2. Therefore, it is recommended that $E_P \propto \sin^{\zeta}\theta$, where the power ζ is closely related to the inconsistency of shale bedding planes caused by the heterogeneity of shale structure. Taking anisotropy of conductivity, the variation of the LIC induced by the residual polarization field effect, ΔI_E, can be described as

$$\Delta I_E \propto \mu \frac{\sigma b}{a} \sin^{\zeta}\theta \propto \mu\sigma \sin^{\zeta}\theta \tag{7}$$

for transverse mode, respectively, where the parameter μ is to be redefined in subsequent equations.

When a bias voltage is supplied, the LIER is enhanced, and the change in LIC due to the V_b was named as ΔI_V. Our research has shown that the selected shale displayed the non-linear I-V curves [19], and the LIC was well described by [19]

$$\Delta I_V \propto c_1 (\Delta T_p)^{c_2} \exp\left(-\frac{c_3}{\Delta T_p}\right)\left[\exp\left(c_4 \frac{V_b}{\Delta T_p}\right) - 1\right] \tag{8}$$

which has similar form with the classical thermionic emission transport relationship, where current density satisfies the formula, $J = J_{ST}[\exp(qV_b/k_bT) - 1] = A_S T^2 \exp(-\Delta\Phi_b/k_bT)[\exp(qV_b/k_bT) - 1]$ [27]. Here, J_{ST} is the saturation current density; A_s the Richardson constant, A·m^{-2}·K^{-2}; T the temperature, K; Φ_b the height of the Schottky barrier in the thermodynamic equilibrium, eV; q the electric charge, A·s; and k_b the Boltzman constant, J·K^{-1} [27]. It can be found that c_2 is dimensionless, and c_1, c_3, c_4 take the forms of A_s, $\Delta\Phi_b/k_b$, q/k_b, respectively. Thus, we can preliminarily assume that $c_1(\Delta T_p)^{c_2}\exp(-c_3/\Delta T_p)$ is the saturation current of shale, and c_3 is closely related the interlayer barrier and coupling in shale since shale is abstracted as a multi-layered dielectric. In fact, due to the complexity of shale structure and composition, although our previous work presented that the semiconductor-like I-V characteristic was shown in shale [19,25], the parameters of c_1~c_3 are not constants as that in the thermionic emission transport relationship, but depend on the laser type, laser power, temperature, and bias voltage. For example, c_1 (A·K^{-1}) is affected by laser power, c_2 and c_4 (K·V^{-1}) are independent of bias voltage and depend on laser power and wavelength, except for c_3 (in the unit of K) which is the constant of the selected material.

Taking $\Delta T_p \propto \alpha$ and Eq. (2), $\Delta T_p \propto PA\kappa_{\perp}^{-1/2}$, Eq. (8) was rewritten in the following form:

$$\begin{aligned}\Delta I_V &\propto \mu_3 \frac{\sigma b}{a}\left(\frac{PA}{\sqrt{\kappa_{\perp}}}\right)^{\mu_4} \\ &\quad \times \exp\left(-\frac{\mu_5\sqrt{\kappa_{\perp}}}{PA}\right)\left[\exp\left(\frac{\mu_6\sqrt{\kappa_{\perp}}V_b}{PA}\right) - 1\right] \\ &\propto \mu_3\sigma\left(\frac{PA}{\sqrt{\kappa_{\perp}}}\right)^{\mu_4}\exp\left(-\frac{\mu_5\sqrt{\kappa_{\perp}}}{PA}\right)\left[\exp\left(\frac{\mu_6\sqrt{\kappa_{\perp}}V_b}{PA}\right) - 1\right]\end{aligned} \tag{9}$$

where the parameters settings of μ_3~μ_6 are to maintain consistency with subsequent equations. It is noted that μ_3~μ_6 directly proportional to c_1~c_4, respectively. By comparison, according to the non-dimensionalization of the exponent index, the units of μ_5 and μ_6 can be obtained as (m·K·W)$^{1/2}$ and (m·K·W)$^{1/2}$·V^{-1}. It can be easily process and obtain that the unit of μ_3 is (m·K·W)$^{-1/2}$·V, and μ_4 is dimensionless. For the sake of convenience, the units of these parameters will be ignored when describing them in subsequent sections.

Thus, ΔI along Electrodes 1 and 2, which is based on the laser-induced thermal effect, the residual polarization electric field effect and the thermal electron emission transport mechanism, is presented as

$$\begin{aligned}\Delta I &= \begin{cases}\Delta I_H - \Delta I_E + \Delta I_V & (\text{Mode 1})\\ \Delta I_H + \Delta I_E - \Delta I_V & (\text{Mode 2})\end{cases}\\ &\propto \begin{cases}\sigma\left\{\frac{PA}{\sqrt{\kappa_{\perp}}} - \mu\sin^{\zeta}\theta + \mu_3\left(\frac{PA}{\sqrt{\kappa_{\perp}}}\right)^{\mu_4}\exp\left(-\frac{\mu_5\sqrt{\kappa_{\perp}}}{PA}\right)\left[\exp\left(\frac{\mu_6\sqrt{\kappa_{\perp}}V_b}{PA}\right) - 1\right]\right\} & (\text{Mode 1})\\ \sigma\left\{\frac{PA}{\sqrt{\kappa_{\perp}}} + \mu\sin^{\zeta}\theta - \mu_3\left(\frac{PA}{\sqrt{\kappa_{\perp}}}\right)^{\mu_4}\exp\left(-\frac{\mu_5\sqrt{\kappa_{\perp}}}{PA}\right)\left[\exp\left(\frac{\mu_6\sqrt{\kappa_{\perp}}V_b}{PA}\right) - 1\right]\right\} & (\text{Mode 2})\end{cases}\end{aligned} \tag{10}$$

and when V_b=0, the laser-induced short-circuit current, ΔI_0, is written as

$$\begin{aligned}\Delta I_0 &= \begin{cases}\Delta I_H - \Delta I_E & (\text{Mode 1})\\ \Delta I_H + \Delta I_E & (\text{Mode 2})\end{cases}\\ &\propto \begin{cases}\sigma\left(\frac{PA}{\sqrt{\kappa_{\perp}}} - \mu\sin^{\zeta}\theta\right) & (\text{Mode 1})\\ \sigma\left(\frac{PA}{\sqrt{\kappa_{\perp}}} + \mu\sin^{\zeta}\theta\right) & (\text{Mode 2})\end{cases}\end{aligned} \tag{11}$$

In this article, we optimize the above model and characterize the anisotropy of shale including the OPA of sliced shale and columnar shale cores under CL and PL irradiations, as well as the evaluation of the laser drilling process.

4. Results

4.1. Anisotropic LIER under CL irradiations

For OPA configuration, Fig. 3a shows the time-dependence of LIER at V_b=0 after 120 s of excitation at 200 and –200 V under an 808 nm CL irradiation with P=3.0 W, which is attributable to the residual transverse polarization electric field. Fig. 3b reviews the dependence of ΔI_0 on P. Regardless of Mode 1 or Mode 2, ΔI_0 has a nonlinear monotonic relationship with P. For example, for Mode 2, with the P from 1.5, 2.0, 2.5, 3.0 to 3.5 W, ΔI_0 at θ=60° increases from 0.55, 1.22, 2.08, 3.68 to 4.51 nA, respectively. The dependency relationship between ΔI_0 and θ is presented in Fig. 3c. For the P ranging from 1.5 to 3.5 W, the ΔI_0 value under Mode 2 is greater than that under Mode 1, e.g., for P=3.5 W and θ=60°, ΔI_0 for Mode 1 and Mode 2 are –2.13 and 4.51 nA, respectively.

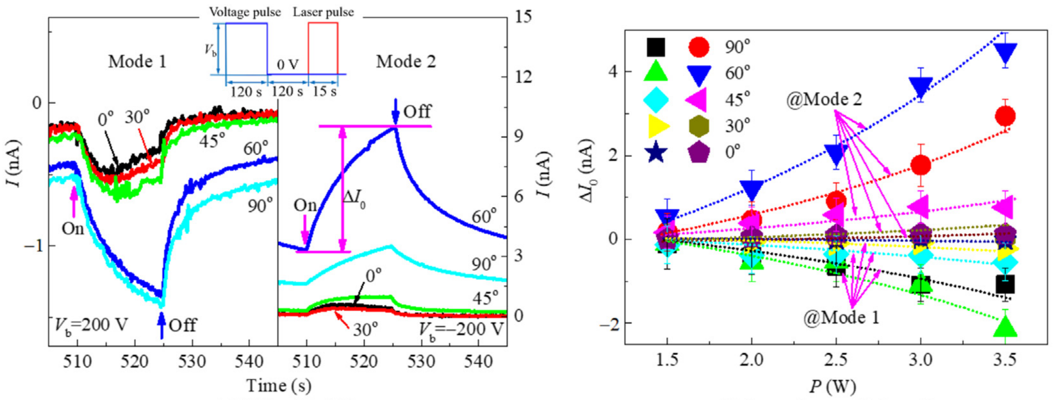

(a) LIC at V_b=0 V

(b) Dependence of ΔI_0 on P

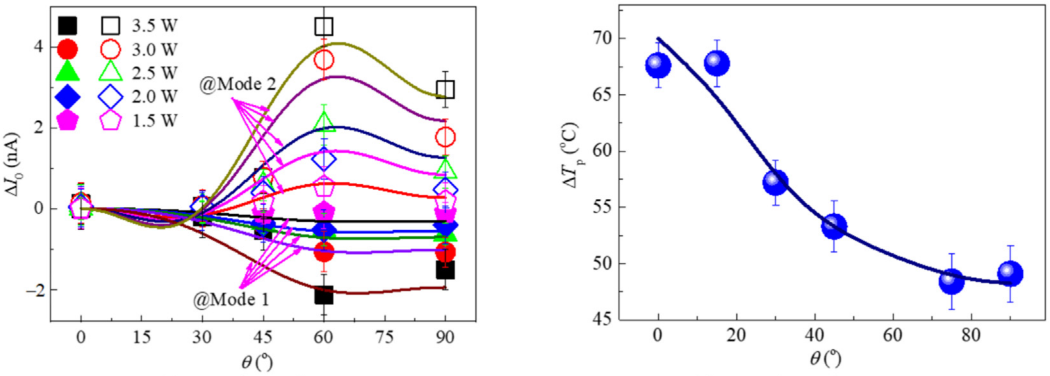

(c) Dependence of ΔI_0 on θ

(d) Dependence of ΔT_p on θ

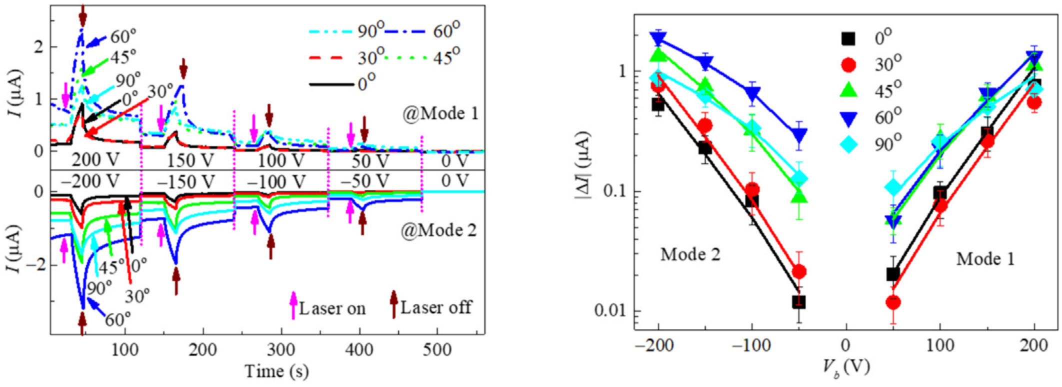

(e) Time-dependence of LIER

(f) Relation of ΔI and V_b

Fig. 3. Anisotropic LIER under 808 nm CL irradiation.

Fig. 3d shows the dependence of surface temperature change ΔT_p at t=t_p on tilting angle θ, which consists well with the relation of $\Delta T_p \propto (4\sin^2\theta+\cos^2\theta)^{-1/2}$, suggesting κ_l/κ_t is about 4 for the selected shale. Nonlinear dependence of the ΔI_0 (Fig. 3b) on the P can be determined as

$$\Delta I_0 \propto \begin{cases} \sigma\left[\frac{PA}{\sqrt{\kappa_\perp}} - \mu_0 (PA)^{\mu_1}\exp\left(-\frac{\mu_2}{PA}\right)\sin^{\zeta}\theta\right] & \text{(Mode 1)} \\ \sigma\left[\frac{PA}{\sqrt{\kappa_\perp}} + \mu_0 (PA)^{\mu_1}\exp\left(-\frac{\mu_2}{PA}\right)\sin^{\zeta}\theta\right] & \text{(Mode 2)} \end{cases} \qquad (12)$$

after taking n_σ=σ_l/σ_t=5, n_κ=κ_l/κ_t=4, ζ=4.0, μ_1=1.1 and μ_2=0.5 with an assumption of the weak dependence of A on tilting angle θ under low power laser irradiation. The second term of Eq. (12), the short-circuit polarization current $\Delta I_{E0} \propto \sigma\mu_0(PA)^{\mu 1}\exp(-\mu_2/PA)\sin^{\zeta}\theta$, is from the residual polarization electric field effect as discussed in Supplementary materials. While the thermionic emission transport relationship is approximately used in shale, it is still obtained through comparison with Eq. (8) that μ_0, μ_1, and μ_2 have physical meanings similar to c_1, c_2, and c_3, since ΔT_p is proportional to P. Thus, the units of μ_0 and μ_2 are V·W^{-1} and W from Eqs. (7) and (12), respectively, with a dimensionless μ_1. μ_0 is independent of P and tilting angle θ, and is 0.228 and 1.822 for Mode 1 and Mode 2. As shown in Fig. 3c, ΔI_0 depends nonmonotonically on θ and has an extremum at θ=60°, which can be fitted well by Eq. (12).

Fig. 3e shows time-dependence LIER with selected tilting angle θ of 0°, 30°, 45°, 60°, and 90° under 808 nm CL irradiation with on-sample power of 3.0 W, where bias voltage V_b is scanned from ±200 to 0 V at intervals of 50 V. The relation of ΔI and V_b is represented in Fig. 3f, and $|\Delta I|$ declines monotonically with the increasement in $|V_b|$, e.g., for θ=90°, ΔI=0.73, 0.51, 0.27, and 0.11 μA at V_b=200, 150, 100, and 50 V, respectively. Fig. 3g illustrates the variation of ΔI with θ under the applied V_b, where the most important feature is

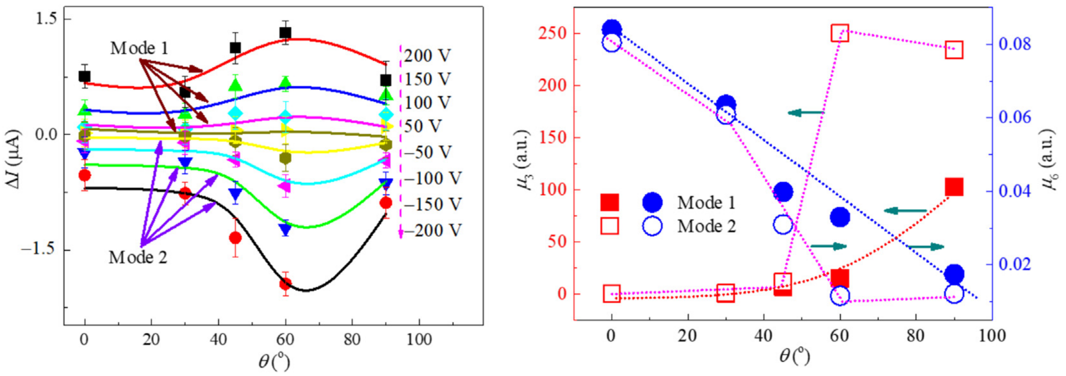

(g) Relation of ΔI and θ

(h) Dependences of μ_3 and μ_6 on θ

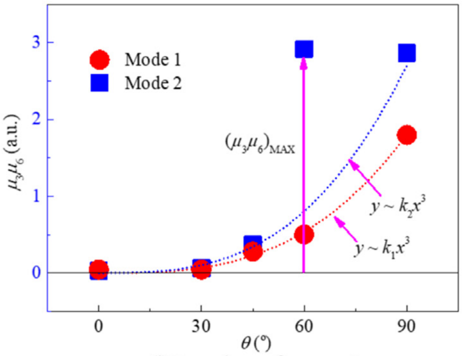

(i) Dependence of $\mu_3\mu_6$ on θ

Fig. 3 (*continued*)

the non-monotonic dependence of ΔI on θ with a maximum value appearing at a threshold angle of θ=60°, e.g., for V_b=200 V, ΔI increases to 1.26 μA with the increasement to 60° in θ, and then decreases to 0.68 at θ=90°.

Comparing the LIER results at V_b=0 V and V_b (Figs. 3a and e), it can be seen that the ΔI_V is much greater than ΔI_0. Thus, following Eq. (10), ΔI is represented as

$$\Delta I \approx \Delta I_V \propto \begin{cases} \mu_3\sigma\left(\frac{PA}{\sqrt{K_\perp}}\right)^{\mu_4}\exp\left(-\frac{\mu_5\sqrt{K_\perp}}{PA}\right)\left[\exp\left(\frac{\mu_6\sqrt{K_\perp}V_b}{PA}\right)-1\right] & (\text{Mode 1}) \\ -\mu_3\sigma\left(\frac{PA}{\sqrt{K_\perp}}\right)^{\mu_4}\exp\left(-\frac{\mu_5\sqrt{K_\perp}}{PA}\right)\left[\exp\left(\frac{\mu_6\sqrt{K_\perp}V_b}{PA}\right)-1\right] & (\text{Mode 2}) \end{cases} \tag{13}$$

The solid lines in Figs. 3f and g are plotted from Eq. (13), taking μ_4=μ_1=1.1, μ_5=μ_2=0.5 and the dependences of μ_3 and μ_6 on θ (Fig. 3h), indicating that the above LIER principle is applicable to the evaluation of anisotropy in shale. As shown in Fig. 3h, μ_3 increases rapidly with θ in exponential form for Mode 1, while increases to 250.5 at θ=60° and then slowly decreases to 234.2 at θ=90° for Mode 2. In contrast, μ_6 linearly depends on θ with a slop of −0.00074 (a.u./(°)) for Mode 1, while declines rapidly from 0.0805 at θ=0° to 0.0116 at θ=60° and then slowly increases to 0.0122 at θ=90° for Mode 2.

It is of considerable importance to discuss the effect of orientation on the given key factors. As displayed in Fig. 3, the LIER for Mode 1 shows lower value than for Mode 2, and also μ_0 for Mode 2 is 8 times higher than that for Mode 1. From the asymmetric current–voltage curve and LIER measurement results, short-circuit current $I_{D0}^{+} > I_{D0}^{-}$ for the whole range of 0°<θ≤90°, indicating the existence of easily polarized directions. Since the highest ΔI_0 and ΔI appear at θ=60°, it is believed that the angle between the easily polarized direction and the bedding plane, named as θ_0, is around 60°.

The calculated $\mu_3\mu_6$ is shown in Fig. 3i, and the data points are fit well using a cubic function, y=kx^3+c, where the coefficient k for Mode 2 is 1.5 times larger than that for Mode 1. Since the LIER of Mode 2 shows an enhanced inflection point at θ=60°, we use the following equation to describe the dependence of $\mu_3\mu_6$ on tiling angle:

$$\mu_3\mu_6 \propto \begin{cases} k_1\theta^3 & (\text{Mode 1}) \\ k_2\theta^3 + \left[(\mu_3\mu_6)_{\mathrm{MAX}} - k_2\theta_0^3\right]\delta(\theta_0) & (\text{Mode 2}) \end{cases} \tag{14}$$

where k_2/k_1=1.5, $\delta(\theta_0)$ is an impulse function with the extreme value $(\mu_3\mu_6)_{\mathrm{MAX}}$ at θ=θ_0. On the other hand, Eq. (12) indicates that the units of μ_3 and μ_6 are $(\mathrm{m{\cdot}K{\cdot}W})^{-1/2}{\cdot}\mathrm{V}$ and $(\mathrm{m{\cdot}K{\cdot}W})^{1/2}{\cdot}\mathrm{V}^{-1}$, respectively, with corresponding dimensions of $\mathrm{L}^{1/2}\mathrm{M}^{1/2}\mathrm{T}^{-2}\mathrm{I}^{-1}$ and $\mathrm{L}^{-1/2}\mathrm{M}^{-1/2}\mathrm{T}^{2}\mathrm{I}$, resulting in a dimensionless product $\mu_3\mu_6$. It is noted that $\mu_3\mu_6$ do not depend on bias voltage and laser power, but strongly on tilting angle. Therefore, it is recommended to refer to $\mu_3\mu_6$ for Modes 1 and 2 as anisotropy factor and easy polarization factor, respectively. Although $\mu_3\mu_6$ is an empirical parameter, this dimensionless product is derived from our theoretical framework based on the above equations, which quantifies the comprehensive effect of electrothermal anisotropy on LIER when laser irradiates shale, indicating its physical significance in coupling the photothermal and electrical characteristics.

4.2. Anisotropic LIER under ns PL irradiations

When a high-frequency ns short laser pulse irradiates the surface of a shale, a significant thermal accumulation effect (TAE) can be induced, thus the LIER become much complicated. Under a ns NIR PL irradiation, the LIC evolutions along the orientation of the electrodes 1 and 2 at V_b=200 V are displayed in Fig. 4a, and b shows time-dependence of LIC at V_b=0 after 120 s of 200 V electric voltage excitation, where the dark current before turning on the laser has already been subtracted. Due to the low thermal conductivity of shale, an obvious TAE induced current $\mathrm{LIC_H}$ is

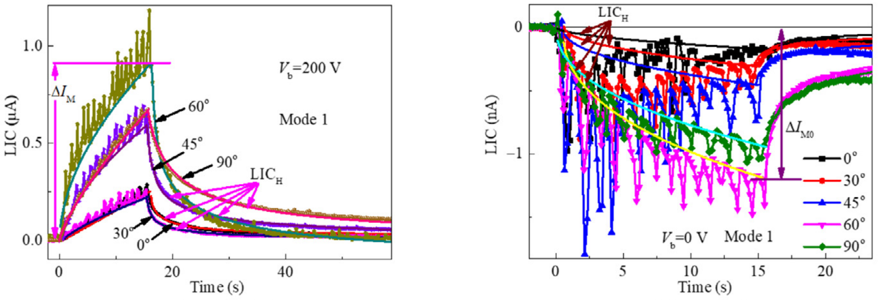

(a) LIC at V_b=200 V

(b) LIC at V_b=0 V

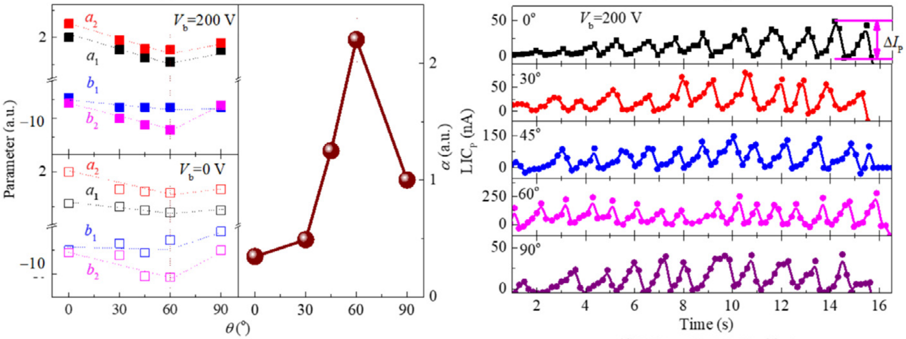

(c) Dependence of fitting factors of LIC$_H$ on θ

(d) LIC$_P$ at V_b=200 V with θ

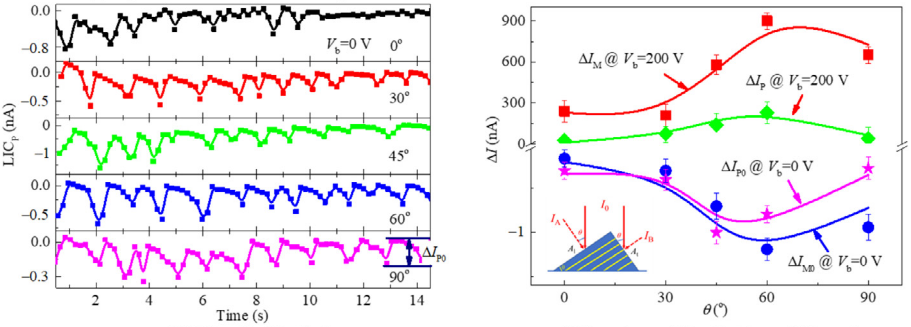

(e) LIC$_P$ at V_b=0 V with θ

(f) Dependence of ΔI_M, ΔI_P, ΔI_{M0}, and ΔI_{P0} on θ

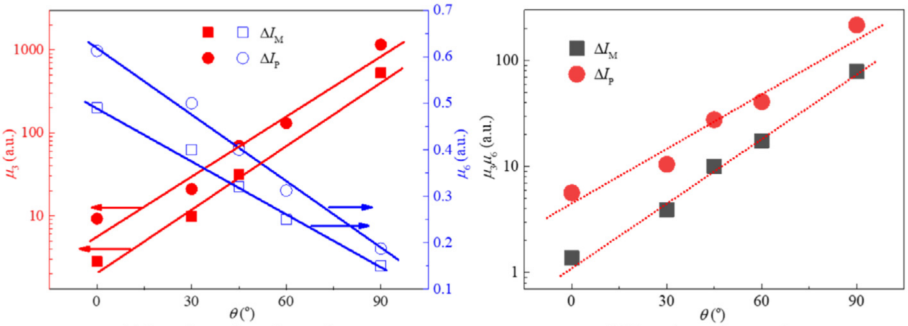

(g) Dependence of μ_3 and μ_6 on θ

(h) Dependence of $\mu_3\mu_6$ on θ

Fig. 4. Anisotropic LIER under a NIR PL irradiation.

seen even at a low laser pulse frequency of 10 Hz. From the measurement result, it can be seen that the LIC quickly rises to a local peak value and then starts dropping. When LIC is still at a high value, the next laser pulse arrives and LIC is driven to another local peak, which is usually higher than the previous peak. This mode is repeated until the last laser pulse, after which the LIC will decrease. Therefore, the measurements indicate that there is a TAE between adjacent laser pulses over time. The LIC$_H$ evolutions are simulated using Eq. (4), where the maxima at laser-off are ΔI_M and ΔI_{M0} under V_b=200 and 0 V. The factors are reviewed in Fig. 4c, where α is independent of V_b, while a_1, a_2, $|b_1|$ and $|b_2|$ for V_b=200 V show higher values than that for V_b=0 V. All parameters present a transition around θ=60°. Furthermore, the LIC$_P$ evolution due to transient laser-thermal effect (TTE), defined as LIC$_P$=LIC−LIC$_H$ (Figs. 4d and e), shows multiple peaks, denoted by ΔI_P and ΔI_{P0} at V_b=200 and 0 V, are the average peak value over the laser pulse irradiation time.

As the interaction time between the ns laser pulse and the shale ranges from ns to μs, whereas the heat diffusion time in the shale is of the order of ms, the surface of shale can be considered as an infinitely thin planar heat source. Thus, the ΔI_H at the end of the laser irradiation time satisfies the following relation:

$$\ln\left(\Delta I_H\right) \propto \ln\left(\Delta T_p\right) \propto \ln\left(\frac{I_L A\sqrt{D_\perp}}{\sqrt{\pi\tau\kappa_\perp}}\right) \propto \ln\left(\frac{I_L A}{\sqrt{\kappa_\perp}}\right) \tag{15}$$

where I_L is laser energy density.

As previous reports the surface of rock can be ablated under an irradiation of ns pulse laser [24,28], resulting in the more rougher surface profile and increasing the tiling angle of microcolumn on the surface [29]. The tilting structure on the surface greatly affects the absorption A. If the incident light is decomposed into two components of vertical and parallel tilting structure surfaces, only the component I_A and I_B perpendicular to the surfaces can cause surface ablation. According to the geometric relationship (inset of Fig. 4f), the A can be represented as [29]

$$\begin{aligned}A(\theta) &\propto \frac{4n\cos^2\theta}{(n^2+k^2)\cos^2\theta+2n\cos\theta+1}+\frac{A_t}{A_l}\frac{4n\sin^2\theta}{(n^2+k^2)\sin^2\theta+2n\sin\theta+1}\\ &= \frac{4n\cos^2\theta}{(n^2+k^2)\cos^2\theta+2n\cos\theta+1}+\gamma\frac{4n\sin^2\theta}{(n^2+k^2)\sin^2\theta+2n\sin\theta+1}\end{aligned} \tag{16}$$

where n is the refractive index, k the complex refractive index, and γ the ratio of absorption A_t in the plane of perpendicular bedding to A_l in the plane of parallel bedding, respectively.

During CL irradiation with low irradiation power density, the shale surface still maintains its bedding characteristics. So, charge carriers mainly migrate along the bedding planes of shale layers, and their motion characteristics are controlled by the dip angle θ of the bedding planes. Thus, the anisotropy of σ is one of the main causes of anisotropy in ΔI_E and ΔI_V. In contrast, when high-energy ns PL vertically irradiates shale, its energy density exceeds the breakdown threshold of shale, causing severe surface ionization and generating plasma plumes, which rapidly expands towards the electrode above the shale surface, causing an instantaneous decrease in impedance. High energy ns PL causes ablation on the surface of shale, and damages the microstructure of the shale surface (such as local melting of bedding planes). The ns PL ablation results in irregular surface structure of shale, thereby the directional dependence of the conductivity relative to θ, detected by the surface electrodes, is weakened. Thus, the influence of anisotropy in σ on LIER, described by Eq. (1), can be approximately neglected under ns PL irradiation.

On the other hand, plasma-induced TTE and TAE greatly increase the velocity of hot carriers in shale, which is strongly influenced by the number of plasmas N_P, enhance the carrier migration rate, and cause the anisotropy of conductivity to be masked by the strong conductivity of plasma channels. Therefore, the ΔI_E and ΔI_V induced by high-energy ns PL are strongly influenced by plasma effects, and the dependence of N_P on θ becomes an indispensable factor. Our previous work suggested that the N_P is approximately proportional to $\sin^3\theta$ [24]. If it is assumed that the dependence of ΔI_E at V_b=0 V on θ is similar to the relationship between ΔI_V and θ, Eq. (10) for Mode 1 under ns PL irradiation is simplified to the following form:

$$\begin{aligned}&\Delta I_M \text{ or } \Delta I_P \propto \frac{I_L A}{\sqrt{\kappa_\perp}}\\ &-\sin^3\theta\left\{\mu_0\left(\frac{I_L A}{\sqrt{\kappa_\perp}}\right)^{\mu_1}\exp\left(-\frac{\mu_2\sqrt{\kappa_\perp}}{I_L A}\right)\right.\\ &\left.-\mu_3\left(\frac{I_L A}{\sqrt{\kappa_\perp}}\right)^{\mu_4}\exp\left(-\mu_5\frac{\sqrt{\kappa_\perp}}{I_L A}\right)\left[\exp\left(\mu_6 V_b\frac{\sqrt{\kappa_\perp}}{I_L A}\right)-1\right]\right\}\end{aligned} \tag{17}$$

and the ΔI_{M0} and ΔI_{P0} when V_b=0 is given by

$$\Delta I_{M0} \text{ or } \Delta I_{P0} \propto \frac{I_L A}{\sqrt{\kappa_\perp}}-\mu_0\sin^3\theta\left(\frac{I_L A}{\sqrt{\kappa_\perp}}\right)^{\mu_1}\exp\left(-\mu_2\frac{\sqrt{\kappa_\perp}}{I_L A}\right) \tag{18}$$

where the parameters settings of μ_0~μ_6 are to maintain consistency with that of Eq. (13).

The dependence trend of ΔI_M and ΔI_{M0} caused by TAE on θ (Fig. 4f) can be simulated using Eqs. (17) and (18), taking γ=3.0, μ_0=1.4, μ_1=μ_4=1.5, μ_2=μ_5=0.04, μ_3 and μ_6 in Fig. 4g. Different from ΔI_{M0} and ΔI_M, ΔI_{P0} and ΔI_P exhibits extreme values at θ=45° and 60° for V_b=0 and 200 V, respectively, which can be simulated by improving μ_0 to 20, μ_2 and μ_5 to 0.09, μ_3 and μ_6 to twice and 1.2 times that of ΔI_{M0} and ΔI_M, in Eqs. (17) and (18). Based on the results, an exponential relationship is provided between $\mu_3\mu_6$ and θ as shown in Fig. 4h, where $\ln\mu_3\mu_6 \propto b\theta$ with the slop b of 0.020 and 0.018 for LIER caused by TAE and TTE. The monotonic dependency relationship between $\mu_3\mu_6$ and θ suggests that the $\mu_3\mu_6$ under PL irradiation can be used as an evaluation index for shale anisotropy.

4.3. Anisotropic tangential LIER on the side of shale core plugs

In this section, we try to apply the OPA model for a cylindrical tight shale with the beddings invisible at different directions. The shale specimen was horizontally cored in the direction parallel with the strata, where the petrophysical bedding plane is perpendicular to the upper and lower surfaces of the core with a 25 mm diameter and 5 cm length. For convenience, a set of electrodes with two 2 mm × 5 cm colloidal silver separated by 30° was equidistantly arrayed on the cylindrical surface of the shale core. The laser irradiates the side of the core vertically along the radial direction. As depicted in Fig. 5a, θ_T is the angle between the current testing direction along two electrodes and the bedding plane. Fig. 5b shows the change in tangential current I_T under an 808 nm CL irradiation with laser power of 3.0 W. At the end of laser irradiation, the LIER change, denoted as ΔI_T, is given by

$$\begin{aligned}\Delta I_T \propto \sigma_T&\left\{\frac{PA}{\sqrt{\kappa_r}}-\mu_0(PA)^{\mu_1}\exp\left(-\frac{\mu_2}{PA}\right)\sin^\zeta\theta_T\right.\\ &\left.+\mu_3\left(\frac{PA}{\sqrt{\kappa_r}}\right)^{\mu_4}\exp\left(-\frac{\mu_5\sqrt{\kappa_r}}{PA}\right)\left[\exp\left(\frac{\mu_6\sqrt{\kappa_r}V_b}{PA}\right)-1\right]\right\}\end{aligned} \tag{19}$$

where radial thermal conductivity

$$\kappa_r = \kappa_l\sin^2\theta_T + \kappa_t\cos^2\theta_T \tag{20}$$

and tangential electrical conductivity

$$\sigma_T = \sigma_l\cos^2\theta_T + \sigma_t\sin^2\theta_T \tag{21}$$

based on the test schematic illustration. The relation between ΔI_T and θ_T is simulated by Eq. (19), which is approximately consistent with the experimental data (Fig. 5c), taking ζ=1.5, μ_0=0.04, μ_1=μ_4=1.1, μ_2=μ_5=0.5, and the dependences of μ_3 and μ_6 on V_b in Fig. 5d. Bias voltage V_b exponentially improves μ_3 following $\mu_3 \propto h_0\exp(h_1V_b)$, where h_0=0.015, h_1=0.013. Although μ_6 drops monotonically from 0.17 to 0.0425 with a V_b from 50 to 200 V, the product h_2 of μ_6 and V_b remains constant of ~8.5. Based on the discussion in Section 3, it can be concluded that the units of h_0, h_1, and h_2 are $(\text{m}\cdot\text{K}\cdot\text{W})^{-1/2}$V, V^{-1}, and $(\text{m}\cdot\text{K}\cdot\text{W})^{1/2}$. Thus, Eq. (19) can be optimized into the following form:

$$\Delta I_T \propto \sigma_T[f_0(P)+f_1(V_b)f_2(P)] \tag{22}$$

where

$$f_0(P) = \frac{PA}{\sqrt{\kappa_r}}-\mu_0(PA)^{\mu_1}\exp\left(-\frac{\mu_2}{PA}\right)\sin^\zeta\theta_T \tag{23}$$

$$f_1(V_b) = h_0\exp(h_1V_b) \tag{24}$$

$$f_2(P) = \left(\frac{PA}{\sqrt{\kappa_r}}\right)^{\mu_1}\exp\left(-\frac{\mu_2\sqrt{\kappa_r}}{PA}\right)\left[\exp\left(\frac{h_2\sqrt{\kappa_r}}{PA}\right)-1\right] \tag{25}$$

The parameters μ_0~μ_2 and h_0~h_2 are independent of bias voltage and laser incidence angle, especially for the current test. Normally, LIER response, which depends on the angle between the measurement direction and the bedding plane, can be effectively enhanced by improving bias voltage and laser power, and the two factors are entangled together in an exponential term of

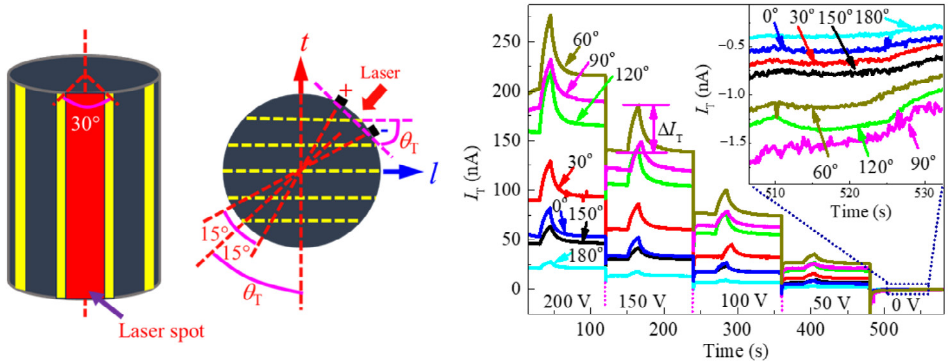

(a) Schematic diagram of the testing method (b) I_T evolution under CL irradiation

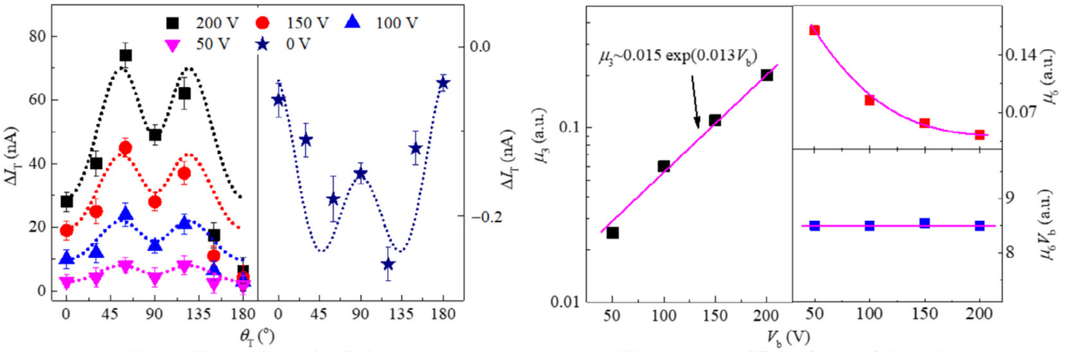

(c) ΔI_T with θ_T under CL irradiation (d) Dependence of fitting factors of ΔI_T on V_b

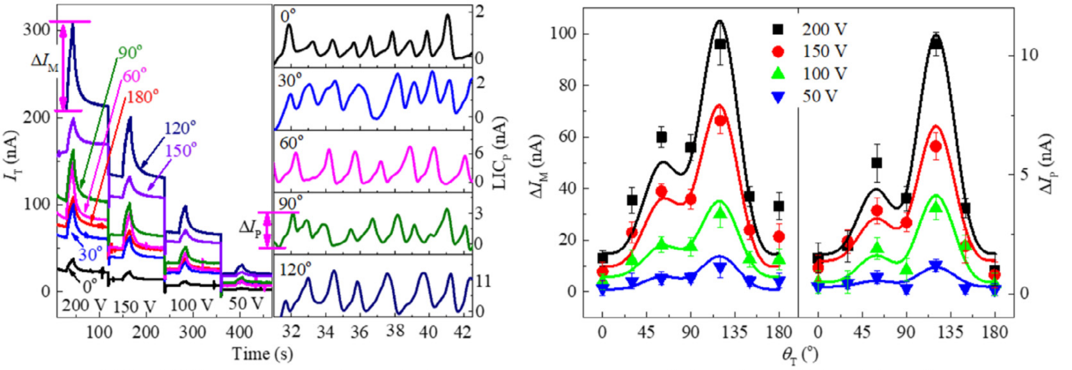

(e) I_T and LIC$_P$ evolutions under PL irradiation (f) Dependence of ΔI_M and ΔI_P on θ_T

Fig. 5. Anisotropic tangential LIER on the side of shale core plugs.

Eq. (13). Here, Eq. (22) indicates that the effects of bias voltage and laser power can be relatively separated as independent variables in three functions of $f_0(P)$, $f_1(V_b)$, and $f_2(P)$, respectively.

Under a ns NIR PL irradiation, the same phenomenon as shown in Figs. 4a and d occurs in the cylindrical tight shale with anisotropic structure (Fig. 5e). The LIC$_P$ evolution can be obtained according to the method introduced in Fig. 4, and the corresponding ΔI_M and ΔI_P due to TAE and TTE are reviewed in Fig. 5f, respectively. After optimizing Eqs. (17) and (22) it is yielded for ΔI_M and ΔI_P with high bias voltage to satisfy the following relationship:

$$\Delta I_M \text{ or } \Delta I_P \propto \sin^3\theta_T \exp(h_1 V_b)\left(\frac{I_L A}{\sqrt{\kappa_r}}\right)^{\mu_1} \times \exp\left(-\frac{\mu_2\sqrt{\kappa_r}}{I_L A}\right)\left[\exp\left(\frac{h_2\sqrt{\kappa_r}}{I_L A}\right)-1\right] \tag{26}$$

taking h_1=0.013, μ_1=1.1 and 1.5 for ΔI_M and ΔI_P, μ_2=0.5, and h_2=0.22, such as the solid fitting lines in the left and right panels of Fig. 5f.

Shale is a sedimentary rock composed of a small amount of semiconductor like components and a large amount of insulating minerals. The arrangement of mineral components and microcracks, interlayer connectivity, organic matter content, and occurrence state are the main factors affecting shale anisotropy. However, the anisotropy mechanism due to shale materials, such as bedding, interfaces, minerals, microcracks, pores and organic matter, has not been clearly defined, and has become a bottleneck issue for LIER to evaluate shale properties. Although our previous research has confirmed the feasibility of LIER technology to characterize shale anisotropy, there is still a lack of a unified and quantitative model as well as evaluation parameters. Here, we separately discussed the laser thermal effect, residual transverse polarization electric field and hot electron emission transport mechanism on LIER, which was fully optimized for laser types (NIR CL and ns PL irradiations) and testing method (OPA). It is noted that LIER data induced by both TAE and TTE are fitted well using current LIER theories. Based on the fitting results, we calculated the products of μ_3 and μ_6 of Eqs. (13) and (17), corresponding to CL irradiation and PL irradiation, respectively, which monotonically changes with θ from 0°–90°. It is clear that the μ_3 and μ_6 are in the same position of three equations, indicating that they can be used as evaluation indices for bedding anisotropy in shale.

Normally, LIER is mainly affected by laser power and bias voltage, which are combined in an exponential term in Eqs. (13) and (17). In cylindrical core testing, the two factors in LIER model of laser power and bias voltage were effectively separated and became three independent variables, which is crucial in the field of engineering evaluation. These results improve the applicability of LIER methods and evaluation parameters in shale oil and gas reservoir evaluation.

4.4. Anisotropic LIER in laser drilling of shale

Pulse laser has the advantages of processing efficiency, reliability, high energy density and flexibility, which can be used as the new tools for drilling oil and gas wells to reduced drilling costs and time with a higher rate of penetration, therefore the use of laser-assisted drilling wells has been widely concerned. Here, we propose a scheme for detecting shale anisotropy during laser drilling process using LIER. The results of Section 4.2 show that ns PL irradiation is largely thermal-induced effects in nature. As presented in Fig. 1d, focusing laser on the local area of shale surface produces more than 5000 times energy density than that in Fig. 4, which creates a strong non-linear effect in the medium. Hence, ns PL irradiation in this work causing many changes such as thermal evaporation, thermal melting, thermal expansion, phase changes, chemical reactions, and plasma impact.

According to the processing method in Fig. 4, we can obtain the LIC evolution along the orientation of the Electrodes 1 and 2 with a tilting angle θ at V_b=200 V under a focused ns NIR PL irradiation (Fig. 6a), where the LIC quickly rises to a local peak value and then starts dropping. Due to the TTE between neighboring laser pulses in time, the LIC signal is driven to another local peak that is typically higher than the previous one at the beginning of period. The LIER curves are effectively separated into two parts of $\mathrm{LIC_H}$ induced by TAE (green line in Fig. 6a) and $\mathrm{LIC_P}$ by TTE (Fig. 6b), respectively, following $\mathrm{LIC_P}$=LIC−$\mathrm{LIC_H}$. There is a turning point at t=t_1 in the $\mathrm{LIC_P}$ evolution curve, where there were significant transient peaks before t=t_1 and then they basically disappeared after that (Fig. 6b). It is known that the drilling depth d increases with irradiation time. Thus, the evolution of LIC can be roughly divided into two stages, taking t=t_1 as the boundary point. In the first stage the d is relatively shallow and the laser mainly acts on the surface of the shale (t<t_1), and in the second stage it is approximately assumed that the plasma is confined within a cylindrical hole at a depth of d (t>t_1).

Unlike mechanical methods, laser drilling technology primarily damages the rock by thermal cracking, melting and vapourisation. The heat transfer between laser and rock is a complex unsteady thermal problem [30]. Here, the ns PL irradiation is simply described as an independent heat source, and the contribution of temperature rise and material evaporation (e.g. plasma) is directly reflected in the LIER model. Different from that for an infinitely thin planar heat source in Eq. (17), the factor $I_L A \kappa_\perp^{-1/2}$ due to laser-thermal effect for focused laser spot should exhibit a lower power exponent φ less than 1. Since the laser focuses on the central area between the electrodes, the hot carrier process in the areas outside the laser spot still follows the classical thermionic emission transport relationship and residual polarization field model in Eq. (17). Thus ΔI_M due to TAE for higher V_b at the end of laser drilling is presented as:

$$\Delta I_M \propto \sigma H - \sigma \sin^3\theta \left\{ \mu_0 H^{\mu_1} \exp\left(-\frac{\mu_2}{H}\right) - \mu_3 H^{\mu_4} \exp\left(-\frac{\mu_5}{H}\right) \left[\exp\left(\frac{\mu_6 V_b}{H}\right) - 1 \right] \right\} \tag{27}$$

where

$$H = \left(\frac{I_L A}{\sqrt{\kappa_\perp}} \right)^{\varphi}, \ \varphi < 1 \tag{28}$$

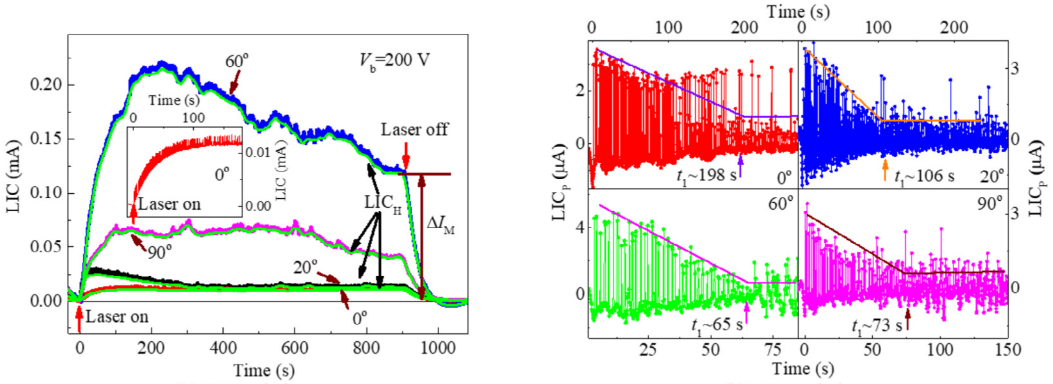

(a) LIC evolution (b) $\mathrm{LIC_P}$ evolution

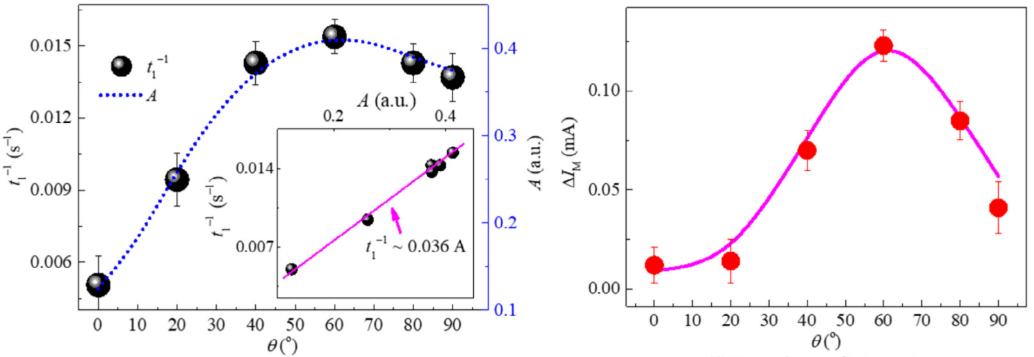

(c) Dependence of t_1^{-1} and A on θ (d) Dependence of ΔI_M on θ

Fig. 6. Anisotropic LIER in laser drilling of shale with selected tilting angle θ under a focused ns NIR PL irradiation at V_b=200 V.

As shown in Fig. 6c, t_1^{-1} and A monotonically increased from 0.0052 s^{-1} and 0.14 at θ=0° to maximum 0.0151 s^{-1} and 0.42 at θ=60°, and then decreases to 0.0133 s^{-1} and 0.37 at θ=90°. The inset of Fig. 6c presents the relation between t_1 and A, satisfying the equation of $t_1^{-1} \propto 0.036A$. A fitting curve of Eq. (27) is obtained, taking φ=0.1, μ_0=0.02, μ_1=μ_4=1.5, μ_2=μ_5=0.5, μ_3=1.1, and μ_6=0.01, based on the above analysis (Fig. 6d).

In general, due to the high peak energy density of ns PL, the multiple complex interfaces in the rock (e.g. solid-liquid mixed interface, solid-gas mixed interface) can absorb or release a large amount of latent heat under ns PL irradiation, resulting in an in-situ time-resolved transient temperature change in the sample [31]. It means that the LIC_P signal is related to the plumes. In this work, the plume is mainly controlled by the physical properties of shale, e.g. the bedding structure. When we remove the transient evolution of heating, melting vaporization and sputtering from the LIER, the signal is mainly affected by the thermal characteristics of shale. Therefore, the LIER is capable of accurately sensing shale bedding structure in real-time during laser drilling process.

5. Discussions

LIER, as a laser technology, has offered valuable solutions and advancements in anisotropy characterization of shale. When shale samples are irradiated by lasers, multiple interaction mechanisms occur, such as the photoelectric effect, photothermal effect, and laser-induced plasma, due to their complex structure and composition. Meanwhile, laser power and bias voltage also affect the LIER results for shale anisotropy. These constraints limited previous studies on shale anisotropy characteristics and origins of LIER. This work establishes LIER detection model for characterizing shale anisotropy and separates the effects of laser power and bias voltage on LIER model. However, the experimental constraints and limitations of LIER technology need to be acknowledged and further investigation are expected.

(1) In this work, the sample is only from a single location. Despite sampling from natural shale, anisotropic geological changes may limit the generality of this model. To address the difficult of the LIER detection model for shale anisotropy, the model will be extended to shales from diverse regions, and LIER detection will be strengthened for marine, transitional, and terrestrial shale's anisotropy in future. It might be necessary to establish a standardized testing plan to obtain a large amount of data, such as improving signal-to-noise ratio, standardizing sample geometry size, optimizing laser types, enhancing detection sensitivity, accelerating scanning and imaging, and strengthening environmental adaptability. In addition, it is expected to develop LIER-based anisotropy prediction models by integrating machine learning with comprehensive experimental datasets.

(2) The present LIER method remains a laboratory-based technique for shale anisotropy characterization, with all experiments conducted under controlled conditions, while emerging as a novel approach relative to traditional technologies. There are many challenges before field implementation. Environmental noise, dust, and beam transmission in complex terrains may compromise LIER response rates during real-world exploration and drilling operations. Additionally, high-energy laser plasma poses ignition risks to reservoir hydrocarbons, which creates a safety hazard for drilling work. Despite challenges from complex geological conditions and multidisciplinary interactions, our present results provide valuable theoretical foundations for practical engineering. Future work can conduct field tests comparing measurements with laboratory results to evaluate LIER's scalability and reliability.

(3) Although LIER can characterize shale anisotropy, LIER detection models lack integration with mechanical, magnetic, or seismic properties. This limitation stems from the fundamental detection mechanisms of LIER technology in this work. LIER model based on thermal and electrical anisotropy has distinct physical mechanisms than the magnetic, seismic, and mechanical anisotropic responses. Meanwhile, laser-shale interactions are governed by numerous interdependent factors including rock composition, crystalline structure, porosity, radiation absorption characteristics and laser parameters. To address this gap, future work will develop a multimodal LIER measurement platform and construct a multi-physics model that links LIER parameters to conventional shale anisotropy indicators through mineralogical characteristics.

The important progress of LIER characterization of shale anisotropy has been achieved in this article, while the research breadth and depth are still lacking, and many challenges need to be solved. Although LIER is still in the initial exploration stage as an emerging technology, we believe that LIER has provided some new insights into the accurate evaluation of shale anisotropy, which will drive the advances of LIER in the exploration for shale oil and gas.

6. Conclusions

In this article, we combined the laser-shale interaction mechanism with electrical measurement, and established the LIER method for characterization and evaluation of shale bedding anisotropy under NIR laser irradiations. The LIER model is further quantified to satisfy the selected engineering scenarios, such as cylindrical tight shale core and laser drilling process of shale. The main conclusions are as follows:

(1) The OPA testing scheme was proposed for LIER of oblique cut shale. Firstly, when the laser beam is vertically irradiated on the surface of oblique cut shale, a temperature gradient is resulted in the irradiation direction (surface normal direction) inside the shale, thereby generating a transverse thermoelectric voltage. Secondly, the bipolar behavior of hysteresis *I-V* curve, as well as the characteristics of laser-induced open-circuit voltage and short-circuit current, indicates the polarization electric field plays a great role in LIER of shale. Thirdly, when a bias voltage is supplied, the LIER is enhanced and described by the classical thermionic emission transport relationship. Thus, the LIER theory and modelling is constructed by the laser-thermal effect, residual transverse polarization electric field effect and thermionic emission transport mechanism, which strongly depends on laser power, bias voltage, and the inclination angle of the measurement direction relative to the bedding plane of shale.

(2) For OPA configuration, LIER depends on the angle θ between the current testing direction and the bedding plane. Under CL irradiation, LIER with or without the applied bias voltage current depends nonmonotonically on θ with a maximum value appearing at a threshold angle of θ=60°, which is consistent with the theoretical model in relation to the tilting angle. In the theoretical simulation parameters of μ_0~μ_6 in the LIER model, only μ_3 and μ_6 depend on θ. The product $\mu_3\mu_6$ is closely related to the θ by a cubic function for Mode

1, while for Mode 2 by the above cubic function and the impulse function that reaches its maximum at θ=60°. It is recommended to use the $\mu_3\mu_6$ as evaluation indicators for shale anisotropy.

(3) When a high-frequency ns short PL irradiates the surface of a shale, a thermal accumulation effect and a transient thermal effect are induced, and are strongly influenced by the number of plasmas which is approximately proportional to $\sin^3\theta$. Due to the ablation of rock surface, the anisotropy of conductivity and polarization electric field can be approximately neglected, and the absorption on the shale surface is related to the inclination angle. Based on these facts, a LIER model under PL irradiation is established, and an exponential relationship is provided between $\mu_3\mu_6$ and θ as $\ln\mu_3\mu_6\propto\theta$. The monotonic dependency relationship between $\mu_3\mu_6$ and θ indicates that the $\mu_3\mu_6$ can be used as an evaluation index for shale anisotropy under PL irradiation.

(4) The LIER model under CL and ns PL irradiations are applied for a cylindrical tight shale with the beddings invisible at different directions. The above models for oblique cut shale are optimized to match the tangential LIER on the side of core plugs. The fitting results are in good agreement with the experimental data with the satisfactory accuracy. The fitting parameter μ_3 is exponentially improved by bias voltage, while the product of parameter μ_6 and bias remains constant of ~8.5. Unlike the model where bias and laser power are exponentially entangled, these two factors by the cylindrical core test are effectively separated, resulting in three independent variables in the optimized LIER model.

(5) Under a focused ns NIR PL irradiation, due to the thermal accumulation and transient thermal effects, the evolution of LIER can be roughly divided into two stages. In the first stage, the drilling depth is relatively shallow, and the laser mainly acts on the shale surface. In the second stage, it is assumed that the plasma is confined within a cylindrical hole at the drilling depth. For focused laser spot, the LIER due to laser-thermal effect exhibits a lower power exponent, and the hot carrier process in the areas outside the laser spot follows the thermionic emission transport relationship and polarization field model. Thus, the LIER due to a thermal accumulation effect at the end of laser drilling is presented well using the present model, suggesting that the LIER is capable to characterize the shale bedding structure in real-time during laser drilling process.

(6) The bottleneck problems that LIER needs to solve in shale physical property characterization include lack of models, inconsistent evaluation parameters, and difficulty in separating influencing factors. The tangential LIER of columnar core specimens not only provides a non-destructive method for anisotropic characterization, but also addresses the entanglement between laser power and bias voltage in the LIER model, which is crucial for laboratory analysis of rock core properties. In drilling process LIER technology can directly quantify the shale anisotropy through the coupling of laser and electricity, thereby eliminating the need for sample extraction and ex-situ analysis. The present study provides a potential in-situ detection method for anisotropic characteristics of reservoir shale during laser drilling, and paves the way for the development of intelligent laser drilling systems for dynamic detection of shale anisotropy.

Acknowledgements

This work was supported by the National Natural Science Foundation of China (Nos. 12374412 and 12404502).

Supplementary material

Supplementary data to this article can be found online at https://doi.org/10.1016/j.ijmst.2025.08.015.

References

[1] Chareonsuppanimit P, Mohammad SA, Robinson Jr RL, Gasem KAM. High-pressure adsorption of gases on shales: Measurements and modeling. Int J Coal Geol 2012;95:34–6.
[2] Dabat T, Hubert F, Paineau E, Launois P, Laforest C, Grégoire B, Dazas B, Tertre E, Delville A, Ferrage E. A general orientation distribution function for clay-rich media. Nat Commun 2019;10:5456.
[3] Zhao LX, Qin X, Zhang JQ, Liu XW, Han DH, Geng JH, Xiong YE. An effective reservoir parameter for seismic characterization of organic shale reservoir. Surveys Geophys 2018;39:509–41.
[4] Zhao J, Wu BS, Jia J, Jiao SX, Yu B, Wu ZG. Shear wave anisotropy response characteristics of laminated shale and its correction methods. Geoenergy Sci Eng 2024;238:212886.
[5] Wang Z, Fan RY, Zong RW, Gong YM. Middle Ordovician bottom current deposits in the western margin of the North China craton: Evidence from sedimentary and magnetic fabrics. Sedimentology 2022;69:1424–55.
[6] Feng Z, Wu HL, Yan WL, Tian H, Zheng JD, Li CL, Wang KW. A new method for quantitative evaluation of shale laminae using electrical image logging. Energy Geosci 2024;5:100274.
[7] Ma T, Liu K, Qiu Y, Liu J, Martyushev DA, Ranjith PG. Quantitative risk assessment of wellbore collapse of inclined wells in formations with anisotropic rock strengths. Rock Mech Rock Eng 2025;58:1795–818.
[8] Zhang QG, Yao BW, Fan XY, Li Y, Fantuzzi N, Ma TS, Chen YF, Zeng FT, Li X, Wang LZ. A failure criterion for shale considering the anisotropy and hydration based on the shear slide failure model. Int J Min Sci Techol 2023;33:447–62.
[9] Blach T, Radlinski AP, Edwards DS, Boreham CJ, Gilbert EP. Pore anisotropy in unconventional hydrocarbon source rocks: A small-angle neutron scattering (SANS) study on the Arthur Creek Formation, Georgina Basin, Australia. Int J Coal Geol 2020;225:103495.
[10] Huang T, Zhai C, Liu T, Sun Y, Xu HX, Wang Y, Huang J. Microstructural evolution and hydraulic response of shale self-propped fracture using X-ray computed tomography and digital volume correlation volume correlation. Int J Min Sci Tech 2025;35:345–62.
[11] Wang WX, Li J, Fan M, Abedi S. Characterization of electrical properties of organic-rich shales at nano/micro scales. Marine Petrol Geol 2017;86:563–72.
[12] Martyushev DA, Ponomareva IN, Davoodi S, Kazemzadeh Y, Kadkhodaie A, Tao Z. Deformation of the void space of pores and fractures of carbonates: Comprehensive analysis of core and field data. Energy Geosci 2025;6 (1):100364.
[13] Ma T, Liu K, Su X, Chen P, Ranjith PG, Martyushev DA. Investigation on the anisotropy of meso-mechanical properties of shale rock using micro-indentation. Bull Eng Geol Environ 2024;83:29.
[14] Xie HP, Hu YQ, Gao MZ, Chen L, Zhang R, Liu T, Gao F, Zhou HW, Peng XB, Li XJ, Li CB, Peng RD, Gao YN, Li C, Li JN, He ZQ. Research progress and application of deep in-situ condition preserved coring and testing. Int J Min Sci Techol 2023;33:1319–37.
[15] Ma RM, Oulton RF. Applications of nanolasers. Nat Nanotechnol 2019;14:12–22.
[16] Miao XY, Zhu J, Li YZ, Zhao K, Zhan HL, Yue WZ. Ultraviolet laser-induced voltage in anisotropic shale. J Phys D Appl Phys 2018;51:045503.
[17] Pan HZ, Hu Y, Kang Y, Chen H, Liu F, Xie JQ, Wang XC. The influence of laser irradiation parameters on thermal breaking characteristics of shale. J Pet Sci Eng 2022;213:110397.
[18] Gowida A, Gamal H, Elkatatny S. Exploring the potential of laser technology in oil well drilling: An overview. Geoenergy Sci Eng 2023;230:212278.
[19] Liu XC, Jiao YQ, Hong Z, Peng X, Lu ZQ, Zhao K, Miao XY. Laser-induced electro-response of oil shale: Principles and applications. Chem Eng J 2024;492:152279.
[20] Miao XY, Zhu J, Zhao K, Yue WZ. Ultraviolet laser-induced lateral photovoltaic response in anisotropic black shale. Appl Phys B 2017;123:276.
[21] Peng X, Miao XY, Liu XC, Lu WT, Zhang SZ, Zhan HL, Yue WZ, Zhao K. Laser-induced voltage of shale due to photothermal effect. Laser Phys 2021;31:096101.
[22] Miao XY, Peng X, Lu WT, Liu XC, Zhang SZ, Zhan HL, Zhao K. A lateral photovoltaic detection for the anisotropic response of invisible-bedding tight shale. Appl Phys B 2020;26:182.
[23] Miao XY, Zhu J, Li YZ, Zhan HL, Zhao K, Yue WZ. Transient laser-induced voltaic response in a partially illuminated dielectric core. Laser Phys 2018;28:086001.
[24] Meng ZH, Chen R, Chen MX, Zhao K, Miao XY, Yue WZ. Probing the anisotropy of shale by the voltaic response of laser-induced plasma. IEEE Trans Instrum Meas 2021;70:7004706.
[25] Liu XC, Miao XY, Zhu MD, Peng X, Lu WT, Zhang SZ, Zhan HL, Yue WZ, Zhao K. Mechanism of the laser-induced voltage generated in oil shale under the irradiation of a 532 nm laser. Energy Fuel 2021;35:1398–403.

[26] Miao XY, Lu WT, Yu YW, Liu XC, Zhan HL, Zhao K. Tunable resistive switching in shales. Results Phys 2023;44:106183.
[27] Racko J, Grmanová A, Breza J. Extended thermionic emission-diffusion theory of charge transport through a Schottky diode. Solid State Electron 1996;39:391–7.
[28] Zhu J, Zhan HL, Zhao K, Miao XY, Zhou Q, Yue WZ. Thermal spallation in rock revealed by ultraviolet laser-induced voltage. Sci China Phys Mech Astron 2019;62:974222.
[29] Conde JC, González P, Lusquiños F, León B. Analysis of the formation and evolution of oriented microstructures on laser ablated silicon. Appl Phys A 2009;95:465–71.
[30] Yan F, Gu YF, Wang YJ, Wang CM, Hu XY, Peng HX, Yao ZL, Wang Z, Shen Y. Study on the interaction mechanism between laser and rock during perforation. Opt Laser Technol 2013;54:303–8.
[31] Yi XZ, Ma WG, Cai ZL, Jiang SZ. Temperature fields characteristics on removal rock by high-energy lasers. AMR 2011;328–330:104–7.